APPLIED PHYSICS

Spontaneous exciton dissociation in transition metal dichalcogenide monolayers

Taketo Handa[1], Madisen Holbrook[2], Nicholas Olsen[1], Luke N. Holtzman[3], Lucas Huber[1]†, Hai I. Wang[4], Mischa Bonn[4], Katayun Barmak[3], James C. Hone[5], Abhay N. Pasupathy[2], Xiaoyang Zhu[1]*

Since the seminal work on MoS_2, photoexcitation in atomically thin transition metal dichalcogenides (TMDCs) has been assumed to result in excitons, with binding energies order of magnitude larger than thermal energy at room temperature. Here, we reexamine this foundational assumption and show that photoexcitation of TMDC monolayers can result in a substantial population of free charges. Performing ultrafast terahertz spectroscopy on large-area, single-crystal TMDC monolayers, we find that up to ~10% of excitons spontaneously dissociate into charge carriers with lifetimes exceeding 0.2 ns. Scanning tunneling microscopy reveals that photocarrier generation is intimately related to mid-gap defects, likely via trap-mediated Auger scattering. Only in state-of-the-art quality monolayers, with mid-gap trap densities as low as 10^9 cm^{-2}, does intrinsic exciton physics start to dominate the terahertz response. Our findings reveal the necessity of knowing the defect density in understanding photophysics of TMDCs.

INTRODUCTION

Excitons in atomically thin two-dimensional (2D) semiconductors, particularly transition metal dichalcogenides (TMDCs), are central to a broad range of problems in 2D materials research. Examples include light-matter interactions (1, 2), optoelectronic processes (3, 4), photocatalysis (5), quantum phases (6, 7), and sensors for quantum phenomena (8–10). In all these examples, photophysical properties of TMDC monolayers are ultimately dictated by whether optical excitation primarily creates excitons (3, 11, 12) or free charge carriers (13–15). Since the seminal work on MoS_2 monolayers (16, 17), photoexcitation in atomically thin TMDCs has been assumed to result in excitons with large binding energies (~200 to 500 meV) (11, 12). Because the exciton binding energies are order of magnitude larger than thermal energy at room temperature, it is puzzling that photocurrent and photovoltage generation have been observed in TMDC-based devices (13–15, 18, 19), even in monolayers with applied electric fields far below the threshold for exciton dissociation (20).

To solve the exciton-versus-carrier puzzle, we apply time-resolved terahertz spectroscopy (TRTS) to investigate the nature of the photoexcited species by providing a contact-free measurement of charge carrier properties (21, 22). Previous studies have applied TRTS to investigate excited-state properties in monolayer TMDCs, but the reported amplitudes, timescales, and even the sign of THz signal vary greatly from report to report (23–27). One complication is that many of these experiments used excitation densities beyond the Mott phase transition, causing excitons to dissociate into electron/hole plasmas (28–30). Moreover, the long wavelength of THz radiation necessitates the use of large-area samples that could previously only be obtained from chemical vapor deposition, which typically yields polycrystalline monolayers with reduced crystalline quality compared to mechanically exfoliated single-crystal monolayers. The preparation of single-crystal TMDC monolayers is crucial when investigating their photophysics because, as we show in the present study, the fate of excitons in TMDC monolayers depends critically on defect density.

RESULTS

We use a gold tape exfoliation technique (31) to prepare single-crystal TMDC monolayers with macroscopic dimensions (millimeter-centimeter). Figure 1Ai shows optical image of a representative single-crystal $MoSe_2$ monolayer; here, the photo is obtained on a Si wafer with 285-nm SiO_2 for enhanced optical contrast. In all spectroscopic measurements, the monolayers are on quartz substrates (see fig. S1 for optical images). The large sizes of the single-crystal monolayers, coupled with a high-sensitivity detection scheme (32), allow us to carry out optical pump–THz probe experiments at excitation densities as low as two orders of magnitude below the Mott threshold. We compare TMDC monolayers (WS_2, WSe_2, $MoSe_2$) exfoliated from single crystals grown by chemical vapor transport (CVT) and the self-flux method. The latter is known to yield single crystals with defect densities order(s) of magnitude lower than those from the former (33). In this experiment, we photoexcite a macroscopic TMDC monolayer and measure the change in optical conductivity with a time-delayed (Δt) THz pulse by recording the real-time waveform E_{THz} via electro-optic sampling (EOS) as a function of timing τ_{EOS} of the electric field (Fig. 1Aii). Fourier transform of the τ_{EOS}-dependent E_{THz} gives a frequency range of ~0.5 to 3.5 THz (Fig. 1Aiii). We excite the TMDC monolayers at photon energy either in resonance or above the 1-s A-exciton transition, as shown by the arrows on the optical absorption spectra obtained for the macroscopic monolayer samples, in Fig. 1B. We keep the excitation densities below the Mott density of ~10^{13} cm^{-2} for TMDC monolayers (29, 30). The THz field predominantly detects charge carriers but not charge-neutral excitons as we discuss below.

[1]Department of Chemistry, Columbia University, New York, NY 10027, USA. [2]Department of Physics, Columbia University, New York, NY 10027, USA. [3]Department of Applied Physics and Applied Mathematics, Columbia University, New York, NY 10027, USA. [4]Max Planck Institute for Polymer Research, Mainz 55128, Germany. [5]Department of Mechanical Engineering, Columbia University, New York, NY 10027, USA.
*Corresponding author. Email: xyzhu@columbia.edu
†Present address: Sensirion AG, Staefa, Switzerland.

Distinct photoconductivity below the Mott threshold in WS₂ monolayers

We first show that in monolayer WS$_2$ exfoliated from a CVT-grown crystal, THz photoconductivity reveals the generation of charge carriers from photoexcitation at photon energies above (green arrow in Fig. 1B) and in resonance with (red arrow in Fig. 1B) the 1-s A-exciton transition (*34*). Figure 1C shows the THz electric field trace, E_{THz}, transmitted through the WS$_2$ monolayer (black dotted curve) and its pump-induced change, ΔE_{THz} (red solid curve). The latter is obtained at absorbed photon density $n_{abs} = 8.5 \times 10^{11}$ cm^{-2} and at pump-probe delay $\Delta t = 5$ ps, with excitation photon energy $h\nu = 2.40$ eV (above-gap). The photoinduced transient ΔE_{THz} tracks the original waveform of E_{THz}, but with flipped sign and with no detectable phase shift, a signature of the spectrally broad absorptive response (*22*). The photoinduced THz field change at peak ΔE_{THz} rises on ultrashort timescales ($\Delta t \leq 1$ ps) following photoexcitation and extends beyond 200 ps (Fig. 1D), with decay time constants in the 20- to 260-ps range (obtained with biexponential fit to data at $\Delta t \geq 10$ ps). The photoinduced complex conductivity spectrum $\Delta\sigma$ (Fig. 1E) obtained from ΔE_{THz} (see Methods) is dominated by the real part, over the entire Δt range (see fig. S2) (*22*). The large exciton binding energy and associated high frequency for intra-exciton Rydberg transitions (*35*) mean that excitons do not contribute to the real part of $\Delta\sigma$ in this frequency range (see note S1 and fig. S3). Hence, the absorption of THz must be free-carrier induced.

We quantify the absolute carrier density through analysis of the complex $\Delta\sigma$ by fitting it to the Drude-Smith model (*36*) at an effective carrier mass of $m_{eff} \sim 0.35\ m_e$ (m_e is the bare electron mass; see Methods) (*37*). The fitting (solid curves in Fig. 1E) gives a carrier density of $n_c = 7.2 \pm 1.0 \times 10^{10}$ cm^{-2} together with the Smith parameter of -0.58 ± 0.05 and scattering time of 49 ± 7 fs. In the Supplementary Materials (note S2 and figs. S4 and S5), we provide a quantitative analysis of the fitting and establish the reliability of carrier density estimation. Accordingly, the fraction of free carriers to the absorbed photon density n_{abs} is calculated to be f_c ($= n_c/n_{abs}$) $= 0.085 \pm 0.011$. As we discuss below, the generation of free carriers likely originates from the trapping of one carrier and the release of a free carrier from an exciton. Thus, f_c is also the fraction of dissociated excitons. Note that the f_c value obtained at $\Delta t = 5$ ps provides a lower limit estimate since ultrafast recombination may occur in this early time window (*38*).

The THz conductivity is observed in a broad range of excitation densities down to 10^{11} cm^{-2} [red open squares (right axis) in Fig. 1F] (also see fig. S6 for the complex conductivity spectra). As shown in fig. S7, the magnitude of the Smith parameter is found to increase with increasing excitation density. As the Smith parameter is considered a measure of carrier localization (*36*), this trend suggests enhanced carrier localization through many-body interaction, which emerges in the vicinity of the Mott transition (see fig. S7 for more discussion). From the fitting shown in fig. S6, we obtain f_c as a function of n_{abs} (filled green circles, left axis in Fig. 1F). Also shown as solid green line is the calculated fraction of exciton dissociation for monolayer WS$_2$ at room temperature from thermodynamic considerations (see Methods and note S3) (*21*). The measured
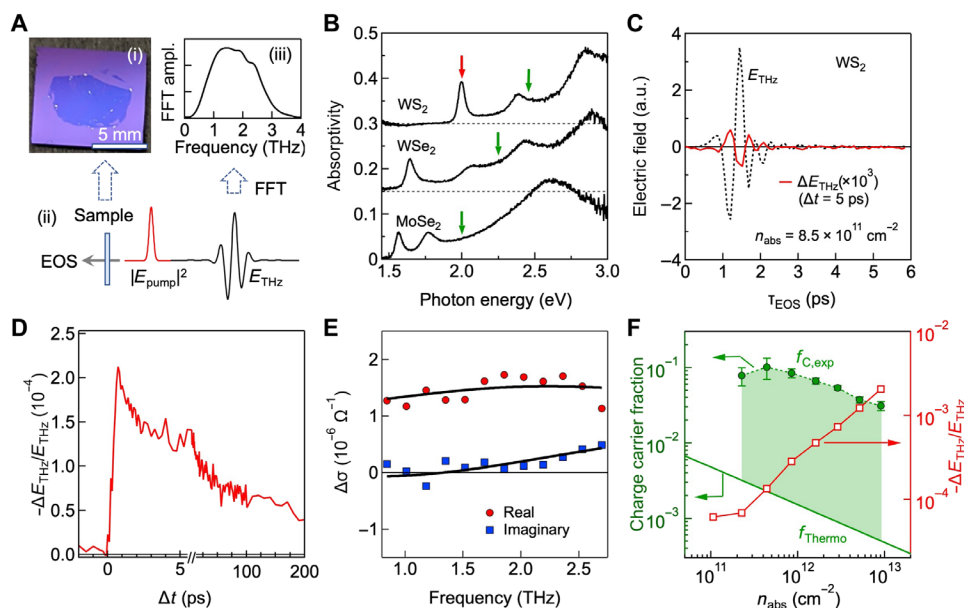
Fig. 1. Observation of charge carriers in photoexcited monolayer WS₂. (**A**) (i) Optical image of representative macroscopic MoSe$_2$ monolayer on SiO$_2$/Si substrate for enhanced optical contrast. (ii) Schematic of experimental setup. Optical pump excites a monolayer TMDC on z-cut quartz, while a time-delayed (Δt) THz probe pulse transmits through the sample and is directed to the EOS system. The real-time THz waveform $E_{THz}(\tau_{EOS})$ is measured by scanning another gate pulse with the timing τ_{EOS}. (iii) Frequency-domain spectrum THz probe obtained via Fourier transform. (**B**) Absorption spectra of TMDC monolayers. The arrows indicate excitation photon energies. (**C**) THz transient (dashed) and its photoinduced change (solid) for CVT WS$_2$ monolayer at absorbed photon density of 8.5×10^{11} cm^{-2} under above-gap excitation. (**D**) Photoconductivity dynamics monitored at the fixed τ_{EOS}, corresponding to the maximum of $-E_{THz}/E_{THz}$ under above-gap excitation. (**E**) Complex photoconductivity spectra together with the fitting result with the Drude-Smith model (see text). (**F**) Excitation density dependence of the maximum THz photoconductivity amplitude (red squares, right axis) and corresponding charge carrier fraction (green circles, left axis). The solid line is the carrier fraction estimated for a perfect monolayer with the thermodynamic Saha equation at 293 K. All experiments were carried out at a sample temperature of 293 K, unless otherwise noted. a.u., arbitrary units.

charge carrier fraction from THz measurement is two orders of magnitude larger (green shaded region) than the thermodynamic prediction for a perfect monolayer.

We confirm the nonthermal origin of the observed THz photoconductivity by measuring $-\Delta E_{THz}/E_{THz}$ (fixed τ_{EOS}) at two temperatures, 293 and 79 K, with above-gap excitation conditions in the CVT WS$_2$ monolayer (Fig. 2A). The amplitudes of photoconductivity and their corresponding f_c values (~0.1) are similar at these two temperatures (see fig. S8). If one considers the thermodynamics of exciton ionization at $T = 79$ K (21), the charge carrier fraction is predicted to be only 10^{-10} to 10^{-11} at the relevant excitation densities (fig. S9). Moreover, we observe clear photoconductivity under resonant excitation of the 1-s A exciton (Fig. 2B). The prompt rise in photoconductivity indicates spontaneous exciton dissociation without the need for excess energy. The real part again dominates the conductivity at different pump-probe delays (Fig. 2C). These results establish that the driving force for exciton dissociation into free charges is not thermal, but likely mediated by an extrinsic process.

Exciton dissociation and mid-gap states in MoSe$_2$ and WSe$_2$ monolayers

To understand the origins of carrier generation in photoexcited TMDC monolayers, we investigate the potential role of mid-gap trap states in meeting the energetic requirements for exciton dissociation (39, 40). Specifically, we compare MoSe$_2$ and WSe$_2$ monolayers exfoliated from crystals grown by CVT and flux methods; defect densities from the latter are known to be order(s) of magnitude lower than those from the former (33, 41). We first focus on MoSe$_2$ and quantify defect density and its electronic structure using scanning tunneling microscopy and spectroscopy (STM and STS) on cleaved bulk crystal surfaces. As established before, quantitative defect analysis of the cleaved crystalline surface provides an excellent proxy to defects in the exfoliated monolayer as determined in photoluminescence spectroscopy (33, 42). Figure 3A shows an STM topographic image of CVT MoSe$_2$, which features bright defects at a density of $n_d = 2.7 \pm 1.2 \times 10^{10}$ cm^{-2}; a magnified image of one such defect is shown in Fig. 3B. For comparison, the density of bright defects in flux-grown MoSe$_2$ is an order of magnitude lower at $n_d = 3.6 \pm 2.5 \times 10^9$ cm^{-2}. While the exact origin of these bright defects is not known, it is a prevalent impurity present in the CVT crystals. STS reveals the presence of mid-gap state on each bright defect feature (red curve in Fig. 3C), similar to the previously reported gap states of defects in MoTe$_2$ and MoS$_2$ (43, 44). Confirming

the occupied nature of these traps, the bright spot only appears in STM image at negative sample bias, not at positive sample bias (fig. S15). For comparison, STS shows no mid-gap state (blue curve in Fig. 3C) when the STM tip is not located on the bright defect of CVT MoSe$_2$. Hence, the flux MoSe$_2$ has less mid-gap defects and is largely trap-free as exemplified by a representative STS (black curve) in Fig. 3C.

The difference in the mid-gap defect densities between the two crystals is reflected in distinct photoinduced THz responses. Figure 3D shows THz time trace, ΔE_{THz} (red curve), at $\Delta t = 10$ ps from the CVT MoSe$_2$ monolayer following above-gap excitation at $h\nu = 2.0$ eV and at an excitation density $n_{abs} = 4.5 \times 10^{12}$ cm^{-2}. The sign reversal from E_{THz} (gray dashed curve, without pump) reflects the positive photoconductivity also observed in the other CVT monolayers of WS$_2$ (Fig. 1C) and WSe$_2$ (shown below in Fig. 4). In stark contrast, ΔE_{THz} from the flux MoSe$_2$ monolayer (blue curve in Fig. 3E) is small but of the same sign as E_{THz} (gray dashed curve), indicating that the transmitted THz field is increased by photoexcitation, i.e., negative photoconductivity. The negative photoconductivity can be attributed to the formation of exciton complexes (24), i.e., exciton polarons commonly referred to as trions (45–47). The MoSe$_2$ monolayer with low defect density from flux grown crystals is known to be n-doped; the free electrons can combine with photogenerated excitons to create negative trions (42). Without photoexcitation, the intrinsically doped electrons in the conduction band absorb THz radiation and reduce the transmitted THz field. Upon photoexcitation, trion formation leads to an increased carrier effective mass, thus reducing THz absorption (24). The negative photoconductivity, represented by $-\Delta E_{THz}/E_{THz}$ (blue dots in Fig. 3F) in the flux MoSe$_2$ monolayer, is characterized by a single exponential recovery (blue fit) with a time constant of ~20 ps, in agreement with the trion recombination time (24). The positive photoconductivity in the CVT monolayer (red dots in Fig. 3F) decays on a similar timescale (~20 ps), but the exponential fit (red curve) reveals a residual signal, i.e., longer-lived carriers attributed to exciton dissociation. These results show that the defect-mediated carrier generation process existing in the CVT monolayers is suppressed in flux-grown monolayers. In the latter, with much lower mid-gap trap density in the 10^{-9} cm^{-2} region, optical excitation results in intrinsic exciton physics. See also fig. S10 comparing the amplitudes of photoconductivity of CVT and flux MoSe$_2$.

The correlation of spontaneous exciton dissociation with mid-gap defect states is also confirmed in WSe$_2$ monolayers from CVT
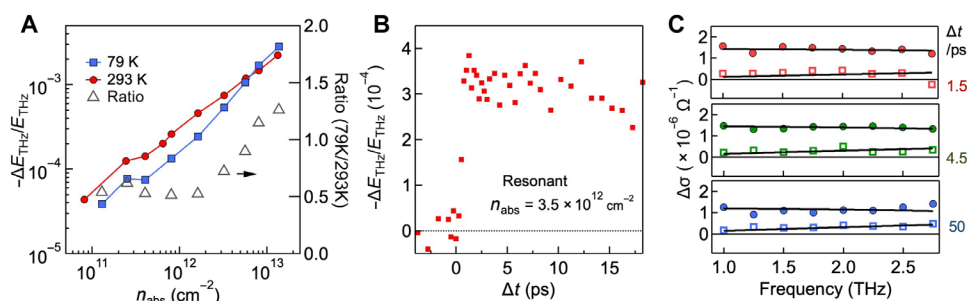
Fig. 2. Nonthermal origin for exciton dissociation in CVT WS$_2$. (**A**) Excitation density dependence of THz photoconductivity amplitude at 293 and 79 K under the above-gap excitation, showing almost temperature-independent conductivity response. (**B**) THz conductivity dynamics following the 1-s resonant excitation. (**C**) Complex conductivity spectra at different pump probe delays, demonstrating that at all delays real part dominates, testifying to the presence of free charges.
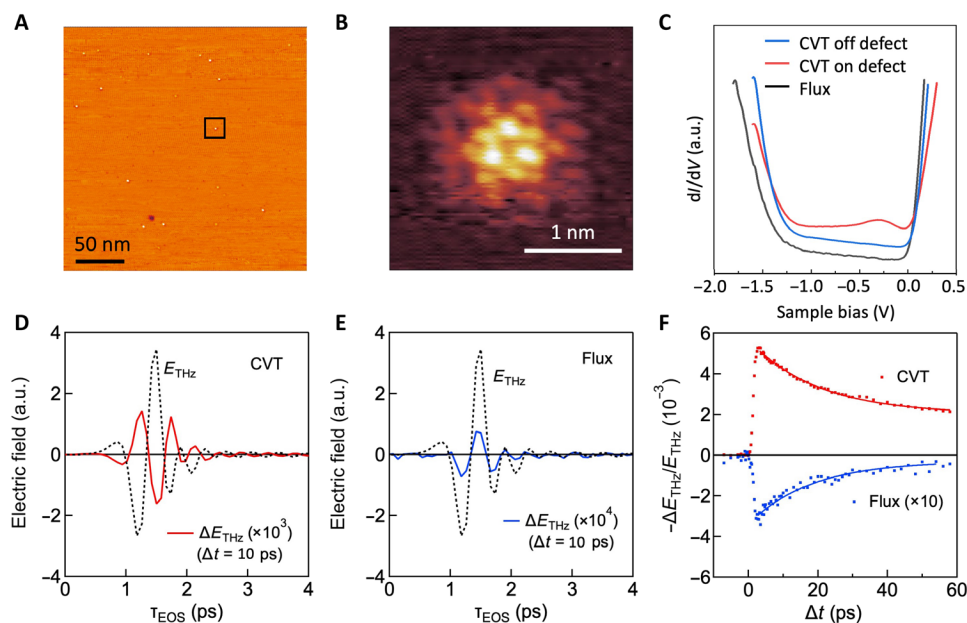
Fig. 3. Mid-gap state induced exciton dissociation in CVT MoSe₂ and trion-induced negative photoconductivity in flux MoSe₂. (**A**) STM topographic image for CVT MoSe₂, showing bright defects. (**B**) A close-up image of the bright defect in (A). STM images in (A) and (B) were obtained at a sample bias of −1.3 and −1.5 V, respectively. (**C**) STS spectra collected on (red) and off (blue) the bright defect in CVT MoSe₂, identifying the existence of mid-gap states on the bright defect. Also shown with black curve is the STS scan for flux-grown MoSe₂. (**D** and **E**) Photoinduced THz transients (solid lines) for CVT and flux MoSe₂ monolayers, respectively, at $\Delta t = 10$ ps with the excitation energy of 2.0 eV (above-gap) and density of 4.5×10^{12} cm⁻². The dotted lines show the E_{THz} waveform. (**F**) THz photoconductivity dynamics as a function of Δt for CVT (red) and flux (blue) MoSe₂. Note that the trace for flux MoSe₂ is multiplied by 10. The solid lines show the fitting curves.
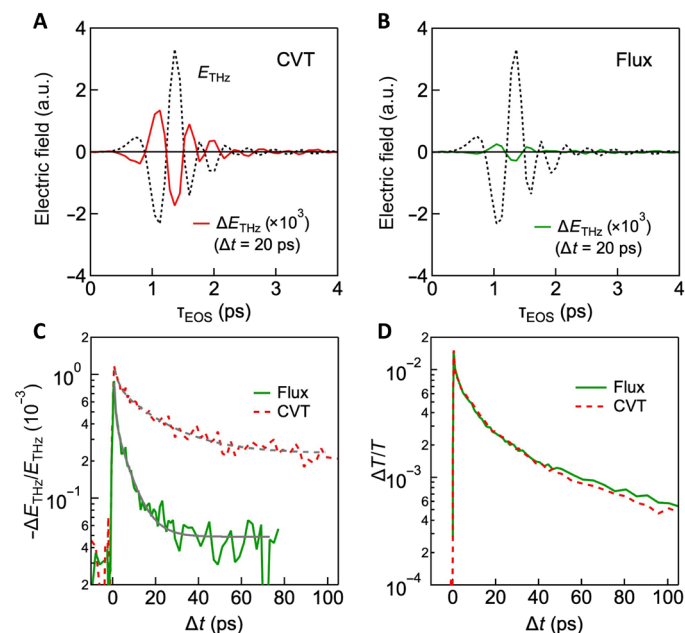
Fig. 4. Intrinsic exciton formation in flux WSe₂. (**A** and **B**) Photoinduced THz transients (solid lines) for CVT and flux WSe₂ monolayers, respectively, at $\Delta t = 20$ ps with the excitation energy of 2.30 eV and density of 5.0×10^{12} cm⁻². The dotted lines show the E_{THz} waveform. (**C**) THz conductivity dynamics for CVT (dotted) and flux (solid) WSe₂ monolayers, showing a faster conductivity decay in flux WSe₂ due to the formation of charge-neutral excitons. The gray curves are fitting results. (**D**) TA bleaching dynamics monitored at the 1-s A-exciton resonance of the same CVT and flux monolayer WSe₂ as THz photoconductivity was measured under the same excitation condition.

and flux-grown WSe₂ crystals, with defect density from the former being one order of magnitude higher than that in the latter (*33, 41*). Figure 4 (A and B) shows THz time traces, ΔE_{THz}, at $\Delta t = 20$ ps from CVT (red) and flux (green) WSe₂ monolayers, respectively, following above-gap excitation at $h\nu = 2.30$ eV and at excitation density $n_{abs} = 5.0 \times 10^{12}$ cm⁻². The THz photoconductivity at $\Delta t = 20$ ps is 8× lower in the flux WSe₂ monolayer (Fig. 4B) than that in the CVT monolayer (Fig. 4A). This difference between the two samples varies strongly with Δt. Figure 4C shows the THz photoconductivity, $-\Delta E_{THz}/E_{THz}$, as a function of delay time for both samples. The $-\Delta E_{THz}/E_{THz}$ values from CVT and flux WSe₂ monolayers are nearly the same immediately following photoexcitation but diverge to a ratio of ~8 at $\Delta t \geq 20$ ps. Specifically, $-\Delta E_{THz}/E_{THz}$ from flux WSe₂ monolayer decays faster on timescales of 0.5 ± 0.1 ps and 5 ± 1 ps (biexponential fit as solid gray curve). For comparison, the signal from CVT monolayer decays on much longer timescales of 1.9 ± 0.2 ps and 20 ± 2 ps (biexponential fit as dashed gray curve). Because the THz probe predominantly detects charge carriers, this result suggests that the population of charge carriers decays more efficiently in the flux WSe₂ monolayer than in the more defective CVT monolayer.

The results in Fig. 4C appear counterintuitive. To understand the origin, we used transient absorption (TA) spectroscopy since it can measure the total population of charge carriers and charge-neutral excitons from the bleaching of the 1-s A-exciton resonance (see fig. S11) (*28, 48*). Figure 4D compares photoinduced bleach ($\Delta T/T$, photoinduced transmission normalized by transmission without excitation), integrated over the 1-s exciton resonance in CVT (red) and flux (green) samples. We use the same excitation condition as TRTS, $h\nu = 2.30$ eV and $n_{abs} = 5.0 \times 10^{12}$ cm⁻², for both monolayers. The

$\Delta T/T$ time profiles are essentially the same, and they deviate from each other only slightly at longer times. Thus, the presence of mid-gap defect states does not contribute appreciably to the overall decay dynamics of electronic excitations [see note S5 for more discussion of bleaching amplitudes arising from excitons and carriers (30, 49)]. Since the TA measurement establishes similar dynamics in both CVT and flux WSe$_2$ monolayers (Fig. 4D), the much faster decay of THz photoconductivity in the latter (Fig. 4C) cannot be due to the decay of the overall electronic excitation. Rather, we attribute the fast decay of THz photoconductivity in the flux WSe$_2$ monolayer on the 0.5- to 5-ps timescale to a change in the identity of the photoexcited species, particularly the formation of insulating excitons from the unbound and conducting electrons and holes formed initially from above-gap excitation (38, 48). With this in mind, the long-lived THz signal in CVT monolayers is attributed to a substantial portion of the electronic excitation remaining as carriers, in contrast to the common view of the dominance of excitons.

DISCUSSION

The THz photoconductivity in CVT monolayer TMDCs is independent of temperature, is correlated with mid-gap trap states, and is observed at sufficiently low excitation density. Defect mediation at the single excitation limit has been proposed before for nonradiative recombination (50), including Auger scattering (39, 40). Figure 5 illustrates the proposed intra-exciton Auger mechanism for exciton dissociation in a TMDC monolayer. We adopt the rigorous energy level diagram based on either ionization energy or electron affinity for both carriers and excitons (Fig. 5) (51). The energy liberated from hole trapping by a mid-gap state can satisfy the energy requirement for exciton dissociation, which releases the free electron into the conduction band in an Auger scattering process (Fig. 5A). The same argument applies to electron trapping and releasing the free hole to the valence band (Fig. 5B). Recent theoretical work suggests that Auger scattering processes are particularly efficient for monolayer TMDCs because the same strong Coulomb potential responsible for large exciton binding energies also leads to high electron/hole trapping and high Auger scattering rates (39, 40). The estimated electron/hole trapping time for an exciton in a TMDC monolayer is

≤1 ps (39). This is the same timescale for the Auger mechanism to release a free electron or hole, in agreement with the observed ultrafast rise in THz photoconductivity.

A large fraction of charge carriers exceeding the Saha consideration has also been suggested in other excitonic semiconductors, namely, 2D lead halide perovskite thin films (52, 53), where polaronic screening in the dynamically disordered lattice and exciton-exciton annihilation at sufficiently high excitation densities have been suggested as possible reasons. These mechanisms are not applicable here for the TMDC monolayers with no dynamic phonon disorders and at excitation densities far below the Mott density. Our combined TRTS and STM/STS studies reveal the critical role of mid-gap states in mediating the dissociation of excitons with large binding energies. This mechanism should be applicable to other 2D semiconductors, including the 2D perovskites, where the Auger-like trap-mediated exciton dissociation is enhanced by the poorly screened Coulomb interactions. Note that we may expect a saturation behavior for free carrier generation with increasing exciton density in a trap-mediated mechanism, but this was not observed in the excitation density range probed here (Fig. 2A). Such saturation behavior may be obscured by other competing many-body scattering events. For example, a charged trap may be freed in another Auger-type nonradiative recombination (39, 40). In addition, the Mott transition from exciton gas to electron-hole plasma is a second-order process (28), and its increasing importance with exciton density may well compensate for the saturation behavior expected for a trap-mediated exciton dissociation mechanism.

Our findings have solved a major conundrum in the photophysics of TMDC monolayers, namely, the seemingly contradicting results on large exciton binding energies and free carrier generation in various optoelectronic devices. These findings also suggest that the common assumption of excitons being the dominant quasiparticle formed in photoexcited TMDC monolayers is only valid in the limit of low defect densities. The fact that ~10% of excitons spontaneously dissociate into carriers in photoexcited TMDC monolayers exfoliated from commonly available CVT crystals indicates that one needs to be cautious when applying the widely held views of exciton physics, especially when defect densities are unknown. For example, in studies of trions in TMDC monolayers (54, 55) and, more recently,
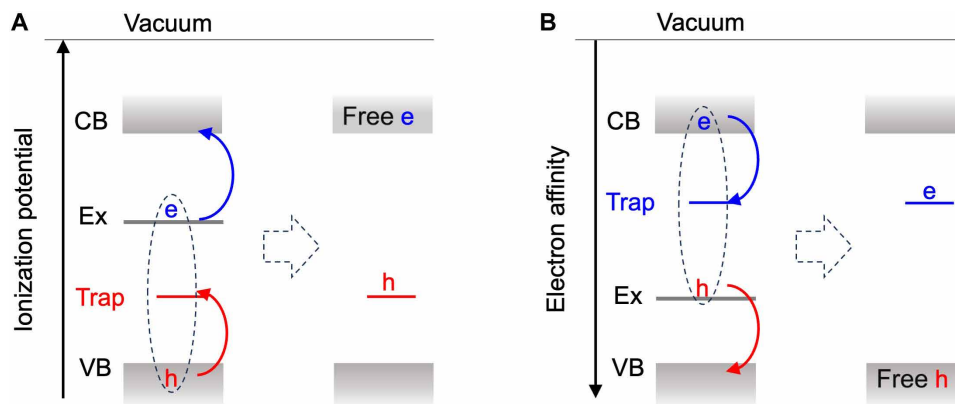
Fig. 5. Defect-mediated exciton dissociation. (**A**) Drawn on the energy scale of ionization potential, the energy of hole trapping to a mid-gap state can satisfy the energy requirement for dissociating the exciton and releasing a free electron to the conduction band. (**B**) Similar diagram for electron trapping and hole releasing on an electron affinity scale. CB (VB), conduction (valence) band; Ex, exciton level.

on exciton-charge mixed quantum phases (56) or trion sensing of quantum phases (57) in TMDC moiré bilayers, the presence of charges is usually assumed to be from intrinsic and/or external electrostatic doping. Our finding of efficient dissociation suggests that charge carriers can also be generated directly from photoexcitation, which may substantially alter the formation kinetics of trions of mixed exciton-charge phases. The process of spontaneous exciton dissociation in the presence of trap states should be of general importance, as the poor screening at the 2D limit not only is responsible for the large exciton binding energy but also enhances any process involving the Coulomb potential. While reducing defect density to reach the intrinsic physical limit is always an important goal in 2D materials research, one may also intentionally incorporate or control these defects for efficient carrier generation in optoelectronics, such as photodetectors.

METHODS

Crystal growth of self-flux crystals

We synthesized MoSe$_2$ and WSe$_2$ crystals using a self-flux method with excess Se (33, 58). Mo (W) powder of 99.997% (99.999%) purity was loaded into a quartz ampule with Se shot of 99.999+% purity in a metal-to-chalcogen molar ratio ranging from 1:5 to 1:100. The ampule was evacuated to ~10^{-5} torr and sealed. The sealed ampule was heated to 1000°C over 24 hours, held at that temperature for 2 weeks, and then cooled at a rate of 1°C/hour to 500°C, at which the cooling rate was increased to 5°C/hour down to room temperature. The ampule was then reheated back to 1000°C over 24 hours, held at that temperature for 5 days, and the same cooling procedure was done down to room temperature. The TMDC and excess selenium contents were transferred to a new quartz ampule, and a piece of quartz wool was added and pushed down to about 1 cm above the TMDC crystals and excess selenium. The second ampule was sealed under vacuum at the aforementioned pressure, heated to 285°C to melt the unreacted Se and dwelled for 30 min, and then removed from the furnace, flipped, and centrifuged. The TMDC crystals were collected from the quartz wool, transferred to a third ampule, and then sealed under vacuum. The crystals were annealed for 24 hours in a temperature gradient with the crystals at the hot end at 285°C, and the cold end of the ampule held at room temperature. The purpose of this annealing step was to melt and remove any excess selenium from the crystals.

Gold tape exfoliation of large-area monolayer TMDs

Macroscopic TMDC monolayers were exfoliated via the gold tape method (31). Bulk WS$_2$, WSe$_2$, and MoSe$_2$, grown via CVT, were purchased from HQ Graphene; flux-grown WSe$_2$ and MoSe$_2$ were grown as described above. Gold tape is prepared by evaporating gold onto a polished silicon wafer before spin coating a protective layer of polyvinylpyrrolidone (PVP). We deposit 150 nm of gold onto the polished silicon wafer at a rate of 0.05 nm/s (Angstrom Engineering EvoVac Multi-Process thin-film deposition system). The PVP protection layer is prepared by spinning a solution of PVP (40,000 molecular weight, Alpha Aesar), ethanol, and acetonitrile with a 2:9:9 mass ratio onto the gold surface of the wafer (1000 rpm, 1000 rpm/s acceleration, 2 min) before curing on a hot plate (150°C, 5 min). Once the gold tape is prepared, it is removed from the silicon wafer using thermal release tape [Semiconductor Equipment Corp. Revalpha RA-95LS(N)]. The gold tape is lightly pressed onto the surface of a bulk TMDC crystal, exfoliating a large-area monolayer, and then onto a 0.5-mm-thick z-cut quartz substrate (MTI Corporation). The sample assembly is heated on a hot plate at 130°C until the thermal release tape goes cloudy and can be easily removed. The sample assembly is soaked in deionized water for 3 hours to remove the PVP protection layer and in acetone for 1 hour to remove any remaining polymer residue. Then, the gold is dissolved by a 5-min bath in an I$_2$/KI gold etchant solution (iodine, 99.99%, Alfa Aesar; potassium iodide, 99.0%, Sigma-Aldrich, and deionized water with a 4:1:40 mass ratio). The sample is soaked in deionized water for 2 hours to remove any residual etchant, rinsed in isopropanol, and dried with N$_2$.

Time-resolved THz spectroscopy

The setup for optical pump-THz probe spectroscopy is schematically illustrated in fig. S12. For the light source, we used a Ti:sapphire regenerative amplifier (RA) with a pulse duration of 30 fs, a repetition rate of 10 kHz, and a wavelength centered at 800 nm (Coherent, Legend). The RA output was split into three beams for THz generation, THz sampling, and optical pump, respectively. The THz probe pulse was generated in a two-color air plasma method, where the fundamental 800-nm beam passes through a beta barium borate (BBO) crystal to generate the frequency doubled beam. Both the fundamental and frequency-doubled beams were focused onto the same point in air, generating a broadband THz probe pulse. The THz beam was collimated by an off-axis parabolic mirror and transmitted through a high-resistivity Si wafer, which blocks the fundamental and frequency-doubled beams while transmitting the THz field. The THz beam was then focused onto a sample mounted in an LN$_2$ flow cryostat, after which it was collimated by another parabolic mirror. High-density polyethylene and Teflon polymer plates were used to filter the optical pump beam while allowing the transmission of the THz probe. The THz probe was then focused onto a 1-mm (110) ZnTe crystal along with another 800-nm sampling beam, by which the real-time waveform of THz electrical field was detected via EOS. Following the ZnTe crystal, the sampling beam passes through a quarter-wave plate and a Wollaston prism, and the split sampling beams were detected on a balance detector (Thorlabs, PDB210A). The amplified signal from the balance detector was integrated with a boxcar integrator (Stanford Research Systems, SR250), and the output was recorded using a data acquisition (DAQ) card (National Instruments, USB-6216).

The femtosecond optical pump beam was generated using a homebuilt noncollinear parametric amplifier pumped by the second harmonic of the Ti:sapphire laser. The center wavelengths were tuned in the range of 500 to 620 nm with enough fluence for the large-area far-field THz measurements. The beam spot sizes at the sample position were determined with a knife-edge method using a photodetector (Thorlabs, DET100A2) and pyroelectric terahertz power detectors (Gentec-EO, THZ9B-BL-DA) equipped with lock-in amplifier (Stanford Research Systems, SR830) for optical pump and THz probe, respectively. In front of the THz power detector, additional polymer filters were used to block the higher-frequency THz beam from entering the detector. The typical spot sizes (1/e diameter in power) were 2 and 0.15 mm for optical pump and THz probe, respectively. The absorbed photon density was determined via $n_{abs} = a_{eff}P_{ex} \times (fAh\nu)^{-1}$, where a_{eff} is the effective absorptivity, P_{ex} is the laser power, f = 5 kHz is the effective repetition rate after the chopper, A is the beam area, and $h\nu$ is the photon energy. The

effective absorptivity was calculated from the convolution of absorptivity spectrum $a(E)$ and pump spectrum $I_{pump}(E)$ $a_{eff} = [\int dE\ a(E) \times I_{pump}(E)]/[\int dE I_{pump}(E)]$. a_{eff} was 0.049 (0.031) for the above-gap (resonant) excitation of WS_2, 0.072 for WSe_2, and 0.043 for $MoSe_2$. We optimized the spatial overlap between the optical pump and THz probe by inserting a Si wafer as a reference (which gave strong signal) and then replaced it with the actual sample. The Si wafer was also used to confirm the sign of photoinduced signal ΔE_{THz}. The relatively high repetition rate of 10 kHz together with the DAQ acquisition scheme (*32*), the use of filters to block optical beams, and the optimization of electronics allowed for high signal to noise ratio. We confirmed that there was no photoinduced THz signal from the SiO_2 substrate by measuring the area without the TMDC monolayer (fig. S13).

Scanning tunneling microscopy/spectroscopy

STM measurements were performed on a commercial Omicron ultrahigh vacuum STM system. Bulk single crystals of $MoSe_2$ and WSe_2 were mounted onto metallic sample holders by vacuum-compatible silver paste (EPO-TEK H20E). Samples were then exfoliated to expose a clean surface and transferred into the STM chamber. A chemically etched tungsten STM tip was conditioned and calibrated on a Au(111) single crystal before the measurements. Measurements were performed at room temperature (300 K).

Photoinduced conductivity spectra

The time-domain THz electric fields obtained from EOS were converted to the frequency-domain spectra $E_{THz}(\omega)$ by Fourier transformation. Complex spectra of the photoinduced conductivity were then obtained under thin-film approximation: $\Delta\sigma(\omega) = -\frac{1+n_{sub}}{Z_0}\frac{\Delta E_{THz}(\omega)}{E_{THz}(\omega)}$. Here, $\Delta E_{THz}(\omega) = E_{THz,\ w/pump}(\omega) - E_{THz,\ w/o\ pump}(\omega)$ is the photoinduced change in the THz field, $Z_0 = 377\ \Omega$ is the vacuum impedance, and n_{sub} is the complex refractive index of the SiO_2 substrate. n_{sub} was determined independently by performing the THz time-domain spectroscopy on the substrate: $n_{sub} = 2.19 + 0i$.

We analyzed the complex photoconductivity spectra $\Delta\sigma(\omega)$ with the Drude-Smith model (*36*), $\Delta\sigma = \frac{ne^2\tau\ /\ m_{eff}}{1-i\omega\tau}\left[1+\frac{c_{DS}}{1-i\omega\tau}\right]$, where n is the carrier density, e is the elementary charge, m_{eff} is the effective mass, τ is the scattering time, ω is the angular frequency, and c_{DS} is the Smith parameter. For the fitting, the effective mass $m_{eff} = (m_e^{-1} + m_h^{-1})^{-1}$ is the average of the electron and hole effective masses reported in (*37*). The real and imaginary parts were fit simultaneously with a global fitting procedure.

Supplementary Materials

This PDF file includes:
Supplementary Notes S1 to S5
Figs. S1 to S15
Tables S1 to S3
References

REFERENCES AND NOTES

1. L. Zhang, F. Wu, S. Hou, Z. Zhang, Y.-H. Chou, K. Watanabe, T. Taniguchi, S. R. Forrest, H. Deng, Van der Waals heterostructure polaritons with moiré-induced nonlinearity. *Nature* **591**, 61–65 (2021).

2. J. Gu, V. Walther, L. Waldecker, D. Rhodes, A. Raja, J. C. Hone, T. F. Heinz, S. Kéna-Cohen, T. Pohl, V. M. Menon, Enhanced nonlinear interaction of polaritons via excitonic Rydberg states in monolayer WSe_2. *Nat. Commun.* **12**, 2269 (2021).

3. E. C. Regan, D. Wang, E. Y. Paik, Y. Zeng, L. Zhang, J. Zhu, A. H. MacDonald, H. Deng, F. Wang, Emerging exciton physics in transition metal dichalcogenide heterobilayers. *Nat. Rev. Mater.* **7**, 778–795 (2022).

4. K. F. Mak, J. Shan, Photonics and optoelectronics of 2D semiconductor transition metal dichalcogenides. *Nat. Photonics* **10**, 216–226 (2016).

5. R. Yang, Y. Fan, Y. Zhang, L. Mei, R. Zhu, J. Qin, J. Hu, Z. Chen, Y. Hau Ng, D. Voiry, S. Li, Q. Lu, Q. Wang, J. C. Yu, Z. Zeng, 2D transition metal dichalcogenides for photocatalysis. *Angew. Chem. Int. Ed. Engl.* **135**, e202218016 (2023).

6. Z. Wang, D. A. Rhodes, K. Watanabe, T. Taniguchi, J. C. Hone, J. Shan, K. F. Mak, Evidence of high-temperature exciton condensation in two-dimensional atomic double layers. *Nature* **574**, 76–80 (2019).

7. Y. Zeng, Z. Xia, R. Dery, K. Watanabe, T. Taniguchi, J. Shan, K. F. Mak, Exciton density waves in Coulomb-coupled dual moiré lattices. *Nat. Mater.* **22**, 175–179 (2023).

8. Y. Xu, S. Liu, D. A. Rhodes, K. Watanabe, T. Taniguchi, J. Hone, V. Elser, K. F. Mak, J. Shan, Correlated insulating states at fractional fillings of moiré superlattices. *Nature* **587**, 214–218 (2020).

9. Y. J. Bae, J. Wang, A. Xu, D. G. Chica, G. M. Diederich, J. Cenker, M. E. Ziebel, Y. Bai, H. Ren, C. R. Dean, M. Delor, X. Xu, X. Roy, A. D. Kent, X. Zhu, Exciton-coupled coherent magnons in a 2D semiconductor. *Nature* **609**, 282–286 (2022).

10. Y. Shimazaki, I. Schwartz, K. Watanabe, T. Taniguchi, M. Kroner, A. Imamoğlu, Strongly correlated electrons and hybrid excitons in a moiré heterostructure. *Nature* **580**, 472–477 (2020).

11. G. Wang, A. Chernikov, M. M. Glazov, T. F. Heinz, X. Marie, T. Amand, B. Urbaszek, Colloquium: Excitons in atomically thin transition metal dichalcogenides. *Rev. Mod. Phys.* **90**, 021001 (2018).

12. N. P. Wilson, W. Yao, J. Shan, X. Xu, Excitons and emergent quantum phenomena in stacked 2D semiconductors. *Nature* **599**, 383–392 (2021).

13. C.-H. Lee, G.-H. Lee, A. M. van der Zande, W. Chen, Y. Li, M. Han, X. Cui, G. Arefe, C. Nuckolls, T. F. Heinz, J. Guo, J. Hone, P. Kim, Atomically thin p–n junctions with van der Waals heterointerfaces. *Nat. Nanotechnol.* **9**, 676–681 (2014).

14. M. M. Furchi, A. Pospischil, F. Libisch, J. Burgdörfer, T. Mueller, Photovoltaic effect in an electrically tunable van der Waals heterojunction. *Nano Lett.* **14**, 4785–4791 (2014).

15. B. W. H. Baugher, H. O. H. Churchill, Y. Yang, P. Jarillo-Herrero, Optoelectronic devices based on electrically tunable p–n diodes in a monolayer dichalcogenide. *Nat. Nanotechnol.* **9**, 262–267 (2014).

16. K. F. Mak, C. Lee, J. Hone, J. Shan, T. F. Heinz, Atomically thin MoS_2: A new direct-gap semiconductor. *Phys. Rev. Lett.* **105**, 136805 (2010).

17. A. Splendiani, L. Sun, Y. Zhang, T. Li, J. Kim, C.-Y. Chim, G. Galli, F. Wang, Emerging photoluminescence in monolayer MoS_2. *Nano Lett.* **10**, 1271–1275 (2010).

18. A. R. Klots, A. K. M. Newaz, B. Wang, D. Prasai, H. Krzyzanowska, J. Lin, D. Caudel, N. J. Ghimire, J. Yan, B. L. Ivanov, K. A. Velizhanin, A. Burger, D. G. Mandrus, N. H. Tolk, S. T. Pantelides, K. I. Bolotin, Probing excitonic states in suspended two-dimensional semiconductors by photocurrent spectroscopy. *Sci. Rep.* **4**, 6608 (2014).

19. P. Chen, T. L. Atallah, Z. Lin, P. Wang, S.-J. Lee, J. Xu, Z. Huang, X. Duan, Y. Ping, Y. Huang, Approaching the intrinsic exciton physics limit in two-dimensional semiconductor diodes. *Nature* **599**, 404–410 (2021).

20. S. Haastrup, S. Latini, K. Bolotin, K. S. Thygesen, Stark shift and electric-field-induced dissociation of excitons in monolayer MoS_2 and hBN/MoS_2 heterostructures. *Phys. Rev. B.* **94**, 041401 (2016).

21. R. A. Kaindl, D. Hägele, M. A. Carnahan, D. S. Chemla, Transient terahertz spectroscopy of excitons and unbound carriers in quasi-two-dimensional electron-hole gases. *Phys. Rev. B.* **79**, 045320 (2009).

22. R. Ulbricht, E. Hendry, J. Shan, T. F. Heinz, M. Bonn, Carrier dynamics in semiconductors studied with time-resolved terahertz spectroscopy. *Rev. Mod. Phys.* **83**, 543–586 (2011).

23. C. J. Docherty, P. Parkinson, H. J. Joyce, M.-H. Chiu, C.-H. Chen, M.-Y. Lee, L.-J. Li, L. M. Herz, M. B. Johnston, Ultrafast transient terahertz conductivity of monolayer MoS_2 and WSe_2 grown by chemical vapor deposition. *ACS Nano* **8**, 11147–11153 (2014).

24. C. H. Lui, A. J. Frenzel, D. V. Pilon, Y.-H. Lee, X. Ling, G. M. Akselrod, J. Kong, N. Gedik, Trion-induced negative photoconductivity in monolayer MoS_2. *Phys. Rev. Lett.* **113**, 166801 (2014).

25. J. K. Gustafson, P. D. Cunningham, K. M. McCreary, B. T. Jonker, L. M. Hayden, Ultrafast carrier dynamics of monolayer WS_2 via broad-band time-resolved terahertz spectroscopy. *J. Phys. Chem. C* **123**, 30676–30683 (2019).

26. S. Xu, J. Yang, H. Jiang, F. Su, Z. Zeng, Transient photoconductivity and free carrier dynamics in a monolayer WS_2 probed by time resolved terahertz spectroscopy. *Nanotechnology* **30**, 265706 (2019).

27. T. Siday, F. Sandner, S. Brem, M. Zizlsperger, R. Perea-Causin, F. Schiegl, S. Nerreter, M. Plankl, P. Merkl, F. Mooshammer, M. A. Huber, E. Malic, R. Huber, Ultrafast nanoscopy of high-density exciton phases in WSe_2. *Nano Lett.* **22**, 2561–2568 (2022).

28. J. Wang, J. Ardelean, Y. Bai, A. Steinhoff, M. Florian, F. Jahnke, X. Xu, M. Kira, J. Hone, X.-Y. Zhu, Optical generation of high carrier densities in 2D semiconductor heterobilayers. *Sci. Adv.* **5**, eaax0145 (2019).

29. A. Steinhoff, M. Florian, M. Rösner, G. Schönhoff, T. O. Wehling, F. Jahnke, Exciton fission in monolayer transition metal dichalcogenide semiconductors. *Nat. Commun.* **8**, 1166 (2017).

30. A. Chernikov, C. Ruppert, H. M. Hill, A. F. Rigosi, T. F. Heinz, Population inversion and giant bandgap renormalization in atomically thin WS_2 layers. *Nat. Photonics* **9**, 466–470 (2015).

31. F. Liu, W. Wu, Y. Bai, S. H. Chae, Q. Li, J. Wang, J. Hone, X.-Y. Zhu, Disassembling 2D van der Waals crystals into macroscopic monolayers and reassembling into artificial lattices. *Science* **367**, 903–906 (2020).

32. C. A. Werley, S. M. Teo, K. A. Nelson, Pulsed laser noise analysis and pump-probe signal detection with a data acquisition card. *Rev. Sci. Instrum.* **82**, 123108 (2011).

33. D. Edelberg, D. Rhodes, A. Kerelsky, B. Kim, J. Wang, A. Zangiabadi, C. Kim, A. Abhinandan, J. Ardelean, M. Scully, D. Scullion, L. Embon, R. Zu, E. J. G. Santos, L. Balicas, C. Marianetti, K. Barmak, X. Zhu, J. Hone, A. N. Pasupathy, Approaching the intrinsic limit in transition metal diselenides via point defect control. *Nano Lett.* **19**, 4371–4379 (2019).

34. Y. Li, A. Chernikov, X. Zhang, A. Rigosi, H. M. Hill, A. M. van der Zande, D. A. Chenet, E.-M. Shih, J. Hone, T. F. Heinz, Measurement of the optical dielectric function of monolayer transition-metal dichalcogenides: MoS_2, $MoSe_2$, WS_2, and WSe_2. *Phys. Rev. B* **90**, 205422 (2014).

35. A. Chernikov, T. C. Berkelbach, H. M. Hill, A. Rigosi, Y. Li, B. Aslan, D. R. Reichman, M. S. Hybertsen, T. F. Heinz, Exciton binding energy and nonhydrogenic Rydberg series in monolayer WS_2. *Phys. Rev. Lett.* **113**, 076802 (2014).

36. N. Smith, Classical generalization of the Drude formula for the optical conductivity. *Phys. Rev. B* **64**, 155106 (2001).

37. A. Kormányos, G. Burkard, M. Gmitra, J. Fabian, V. Zólyomi, N. D. Drummond, V. Fal'ko, **k·p** theory for two-dimensional transition metal dichalcogenide semiconductors. *2D Mater.* **2**, 022001 (2014).

38. P. Steinleitner, P. Merkl, P. Nagler, J. Mornhinweg, C. Schüller, T. Korn, A. Chernikov, R. Huber, Direct observation of ultrafast exciton formation in a monolayer of WSe_2. *Nano Lett.* **17**, 1455–1460 (2017).

39. H. Wang, J. H. Strait, C. Zhang, W. Chan, C. Manolatou, S. Tiwari, F. Rana, Fast exciton annihilation by capture of electrons or holes by defects via Auger scattering in monolayer metal dichalcogenides. *Phys. Rev. B* **91**, 165411 (2015).

40. H. Wang, C. Zhang, F. Rana, Ultrafast dynamics of defect-assisted electron–hole recombination in monolayer MoS_2. *Nano Lett.* **15**, 339–345 (2015).

41. D. Rhodes, S. H. Chae, R. Ribeiro-Palau, J. Hone, Disorder in van der Waals heterostructures of 2D materials. *Nat. Mater.* **18**, 541–549 (2019).

42. B. Kim, Y. Luo, D. Rhodes, Y. Bai, J. Wang, S. Liu, A. Jordan, B. Huang, Z. Li, T. Taniguchi, K. Watanabe, J. Owen, S. Strauf, K. Barmak, X. Zhu, J. Hone, Free trions with near-unity quantum yield in monolayer $MoSe_2$. *ACS Nano* **16**, 140–147 (2022).

43. Z. Guguchia, A. Kerelsky, D. Edelberg, S. Banerjee, F. von Rohr, D. Scullion, M. Augustin, M. Scully, D. A. Rhodes, Z. Shermadini, H. Luetkens, A. Shengelaya, C. Baines, E. Morenzoni, A. Amato, J. C. Hone, R. Khasanov, S. J. L. Billinge, E. Santos, A. N. Pasupathy, Y. J. Uemura, Magnetism in semiconducting molybdenum dichalcogenides. *Sci. Adv.* **4**, eaat3672 (2023).

44. B. Schuler, J.-H. Lee, C. Kastl, K. A. Cochrane, C. T. Chen, S. Refaely-Abramson, S. Yuan, E. van Veen, R. Roldán, N. J. Borys, R. J. Koch, S. Aloni, A. M. Schwartzberg, D. F. Ogletree, J. B. Neaton, A. Weber-Bargioni, How substitutional point defects in two-dimensional WS_2 induce charge localization, spin–orbit splitting, and strain. *ACS Nano* **13**, 10520–10534 (2019).

45. D. K. Efimkin, A. H. MacDonald, Many-body theory of trion absorption features in two-dimensional semiconductors. *Phys. Rev. B.* **95**, 035417 (2017).

46. M. Sidler, P. Back, O. Cotlet, A. Srivastava, T. Fink, M. Kroner, E. Demler, A. Imamoglu, Fermi polaron-polaritons in charge-tunable atomically thin semiconductors. *Nat. Phys.* **13**, 255–261 (2017).

47. F. Rana, O. Koksal, C. Manolatou, Many-body theory of the optical conductivity of excitons and trions in two-dimensional materials. *Phys. Rev. B* **102**, 85304 (2020).

48. F. Ceballos, Q. Cui, M. Z. Bellus, H. Zhao, Exciton formation in monolayer transition metal dichalcogenides. *Nanoscale* **8**, 11681–11688 (2016).

49. S. Schmitt-Rink, D. S. Chemla, D. A. B. Miller, Theory of transient excitonic optical nonlinearities in semiconductor quantum-well structures. *Phys. Rev. B* **32**, 6601–6609 (1985).

50. P. Li, C. Robert, D. Van Tuan, L. Ren, M. Yang, X. Marie, H. Dery, Intervalley electron-hole exchange interaction and impurity-assisted recombination of indirect excitons in WS_2 and WSe_2 monolayers. *Phys. Rev. B* **106**, 085414 (2022).

51. X.-Y. Zhu, How to draw energy level diagrams in excitonic solar cells. *J. Phys. Chem. Lett.* **5**, 2283–2288 (2014).

52. A. Burgos-Caminal, E. Socie, M. E. F. Bouduban, J.-E. Moser, Exciton and carrier dynamics in two-dimensional perovskites. *J. Phys. Chem. Lett.* **11**, 7692–7701 (2020).

53. S. G. Motti, M. Kober-Czerny, M. Righetto, P. Holzhey, J. Smith, H. Kraus, H. J. Snaith, M. B. Johnston, L. M. Herz, Exciton formation dynamics and band-like free charge-carrier transport in 2D metal halide perovskite semiconductors. *Adv. Funct. Mater.* **33**, 2300363 (2023).

54. J. S. Ross, S. Wu, H. Yu, N. J. Ghimire, A. M. Jones, G. Aivazian, J. Yan, D. G. Mandrus, D. Xiao, W. Yao, X. Xu, Electrical control of neutral and charged excitons in a monolayer semiconductor. *Nat. Commun.* **4**, 1474 (2013).

55. K. F. Mak, K. He, C. Lee, G. H. Lee, J. Hone, T. F. Heinz, J. Shan, Tightly bound trions in monolayer MoS_2. *Nat. Mater.* **12**, 207–211 (2013).

56. H. Park, J. Zhu, X. Wang, Y. Wang, W. Holtzmann, T. Taniguchi, K. Watanabe, J. Yan, L. Fu, T. Cao, D. Xiao, D. R. Gamelin, H. Yu, W. Yao, X. Xu, Dipole ladders with large Hubbard interaction in a moiré exciton lattice. *Nat. Phys.* **19**, 1286–1292 (2023).

57. J. Cai, E. Anderson, C. Wang, X. Zhang, X. Liu, W. Holtzmann, Y. Zhang, F. Fan, T. Taniguchi, K. Watanabe, Y. Ran, T. Cao, L. Fu, D. Xiao, W. Yao, X. Xu, Signatures of fractional quantum anomalous Hall states in twisted $MoTe_2$. *Nature* **622**, 63–68 (2023).

58. S. Liu, Y. Liu, L. N. Holtzman, B. Li, M. Holbrook, J. Pack, T. Taniguchi, K. Watanabe, C. R. Dean, A. Pasupathy, K. Barmak, D. A. Rhodes, L. Fu, J. Hone, Two-step flux synthesis of ultrapure transition-metal dichalcogenides. *ACS Nano* **17**, 16587–16596 (2023).

59. T. G. Pedersen, Exciton Stark shift and electroabsorption in monolayer transition-metal dichalcogenides. *Phys. Rev. B* **94**, 125424 (2016).